Revision 2

Louisfuchsite, $Ca_2(Mg_4Ti_2)(Al_4Si_2)O_{20}$, a new rhönite-type mineral from the NWA 4964 CK meteorite: A refractory phase from the solar nebula

CHI MA[1,*], ALEXANDER N. KROT[2], KAZUHIDE NAGASHIMA[2], TASHA DUNN[3]

[1]Division of Geological and Planetary Sciences, California Institute of Technology, Pasadena, CA 91125, USA

[2]Hawai'i Institute of Geophysics and Planetology, University of Hawai'i at Mānoa, Honolulu, HI 96822, USA

[3]Department of Geology, Colby College, Waterville, Maine 04901, USA

ABSTRACT

Louisfuchsite (IMA 2022-024), with an end-member formula $Ca_2(Mg_4Ti_2)(Al_4Si_2)O_{20}$, is a new refractory mineral identified in a Ca-Al-rich inclusion (CAI) from the NWA 4964 CK3.8 carbonaceous chondrite. Louisfuchsite occurs with spinel, perovskite, grossmanite, plus secondary rutile, titanite, and ilmenite in three regions in the CAI. The mean chemical composition of type louisfuchsite by electron probe microanalysis is (wt%) Al_2O_3 25.48, SiO_2 18.40, MgO 17.92, TiO_2 15.36, Ti_2O_3 3.13, CaO 14.92, FeO 3.30, V_2O_3 0.67, Cr_2O_3 0.08, total 99.26, giving rise to an empirical formula of $Ca_{2.00}(Mg_{3.44}Ti^{4+}_{1.49}Fe_{0.36}Ti^{3+}_{0.34}Al_{0.24}V^{3+}_{0.07}Ca_{0.06}Cr_{0.01})_{\sum 6.01}(Al_{3.63}Si_{2.37})_{\sum 6.00}O_{20}$.

Louisfuchsite has the $P\bar{1}$ rhönite structure with a = 10.37(1) Å, b = 10.76(1) Å, c = 8.90(1) Å, α = 106.0(1)°, β = 96.0(1)°, γ = 124.7(1)°, V = 741(2) Å^3, and Z = 2, as revealed by electron back-scatter diffraction. The calculated density using the measured composition is 3.44 g/cm^3. Louisfuchsite is a new refractory phase from the solar nebula, crystallized from an ^{16}O-rich ($\Delta^{17}O \sim -24\pm2$‰) refractory melt with the initial $^{26}Al/^{27}Al$ ratio of $(5.01\pm0.24)\times10^{-5}$ under reduced conditions. The mineral name is in honor of Louis Fuchs (1915–1991), a mineralogist at Argonne National Laboratory, for his many contributions to research on mineralogy of meteorites.

Keywords: Louisfuchsite, $Ca_2(Mg_4Ti_2)(Al_4Si_2)O_{20}$, new mineral, rhönite subgroup, refractory mineral, Ca-Al-rich inclusion, NWA 4964, carbonaceous chondrite

---

*E-mail: chima@caltech.edu

INTRODUCTION

During a mineralogical investigation of the NWA 4964 meteorite, a refractory Al-rich and Ti-bearing rhönite-type mineral, $Ca_2(Mg_4Ti_2)(Al_4Si_2)O_{20}$ with the $P\bar{1}$ aenigmatite structure, named "louisfuchsite", was identified in a coarse-grained igneous Compact Type A (CTA) Ca-Al-rich inclusion (CAI) named NWA 4964 #1 (Fig. 1). The NWA 4964 meteorite, found in 2007 from Northwest Africa, is a CK3.8 (Karoonda type) carbonaceous chondrite. CTA CAIs are one major type of coarse-grained refractory inclusions in carbonaceous chondrites, formed in the solar nebula (Simon et al. 1999).

This Al-rich and Ti-bearing rhönite was previously observed in some Allende CAIs (Fuchs 1971, 1978; Bonaccorsi et al. 1990), but not submitted for IMA approval. According to the nomenclature of the sapphirine supergroup, this Allende rhönite is classified as unnamed under the rhönite subgroup (Grew et al. 2018). The IMA-CNMNC has approved this phase from NWA 4964 as a new mineral based on our proposal (IMA 2022-024; Ma and Krot 2022). The mineral name is in honor of Louis Fuchs (1915–1991), a mineralogist at Argonne National Laboratory, for his many contributions to research on mineralogy of meteorites, who first observed this mineral in the Allende CV3 meteorite. The Allende rhönite reported by Fuchs (1971, 1978) is louisfuchsite. We describe here the occurrence of louisfuchsite in NWA 4964, as a refractory mineral, and discuss its origin and significance for understanding nebular processes in the early solar system.

Louisfuchsite ($Ca_2(Mg_4Ti_2)(Al_4Si_2)O_{20}$) is a new member of the rhönite subgroup (Ca-dominant) in the sapphirine supergroup. The general crystal chemical formula of the rhönite subgroup is $Ca_2M_6T_6O_{20}$, where M = Mg,Al,Ti^{4+},Ti^{3+},Fe^{2+},Fe^{3+},Sc,V^{3+},Cr,Zr, T = Si,Al. Louisfuchsite has Al > Si in the T sites so it is the Al-analog of rhönite ($Ca_2(Mg_4Fe^{3+}Ti)(Si_3Al_3)O_{20}$). Louisfuchsite has Mg dominated in the M sites so it is also the Mg-analog of addibischoffite ($Ca_2Al_6Al_6O_{20}$), warkite ($Ca_2Sc_6Al_6O_{20}$) and beckettite ($Ca_2V_6Al_6O_{20}$). Addibischoffite, warkite and beckettite are also refractory phases recently-discovered in CAIs in carbonaceous chondrites (Ma et al. 2017, 2020, 2021).

SAMPLE AND METHODS

The holotype material of louisfuchsite in NWA 4964 section is in the Meteorite Collections at the Department of Geology, Colby College, Waterville, Maine 04901, USA, registration number NWA 4964A.

Electron probe microanalyzer (EPMA), field emission scanning electron microscope (SEM) and electron back-scatter diffraction (EBSD) have been used to characterize composition and structure of louisfuchsite. Backscattered electron (BSE) imaging was performed using a ZEISS 1550VP field emission SEM. Quantitative elemental microanalyses were carried out using a JEOL 8200 EPMA (WDS mode, 10 kV, 15 nA, focused beam mode). Standards were anorthite (Si*K*α, Al*K*α, Ca*K*α), TiO_2 (Ti*K*α), fayalite (Fe*K*α), forsterite (Mg*K*α), Cr_2O_3 (Cr*K*α), and V_2O_5 (V*K*α). Analyses were processed with the CITZAF correction procedure (Armstrong 1995). Analytical results are given in Table 1.

Electron backscatter diffraction (EBSD) analyses at a sub-micrometer scale were performed using methods described in Ma and Rossman (2008, 2009). An HKL EBSD system on a ZEISS 1550VP SEM, was operated at 20 kV and 6 nA in focused beam mode with a 70º tilted stage and in a variable pressure mode (25 Pa). The focused electron beam is several nanometers in diameter. The spatial resolution for diffracted backscattered electrons is ~30 nm in size. The EBSD system was calibrated using a single-crystal silicon standard. The structure was determined and cell constants were obtained by matching the experimental EBSD patterns with structures of aenigmatite, rhönite, serendibite, krinovite, and makarochkinite.

Oxygen-isotope compositions in louisfuchsite and other primary and secondary minerals in the CAI NWA 4964 #1 were measured in situ with the UH Cameca ims-1280 secondary ion mass spectrometer (SIMS) using two different analytical protocols that are similar to those in Nagashima et al. (2015). Prior to oxygen isotopic measurements, the grains of interest were marked by electron beam using JEOL LV5900 SEM (for details, see Nagashima et al. 2015). For coarse grains (>15 μm in smallest dimension), a focused ~1.2 nA primary Cs^+ ion beam rastered over a 10×10 μm and a 7×7 μm area was used for presputtering and data collection, respectively. Secondary ions of $^{16}O^-$, $^{17}O^-$, and $^{18}O^-$ were measured simultaneously in multicollection mode with the magnetic field controlled by a nuclear magnetic resonance (NMR) probe. $^{16}O^-$ and $^{18}O^-$ were measured by multicollector Faraday cups (FCs) with low mass resolving power (MRP ~ 2000), while $^{17}O^-$ was measured using the axial monocollector electron multiplier (EM) with MRP of ~5600, sufficient to separate the interfering $^{16}OH^-$ signal. The $^{16}OH^-$ signal was monitored during each measurement and was typically less than 1×10^6

cps, while typical $^{17}O^-$ count rate was ~2.5×10^5 cps. Contribution of $^{16}OH^-$ onto $^{17}O^-$ was corrected based on a peak/tail ratio. The correction was less than 0.05‰. Due to the relatively high $^{17}O^-$ signal on the axial EM, a detection efficiency change of the EM is often a big problem as it affects measured $\Delta^{17}O$. We have developed a way to monitor the detection efficiency during measurement, following the technique developed for Mg-isotope measurements by Kita et al. (2018) and Siron et al. (2021). The output from an amplifier for the axial EM was divided and input to two discriminators, one for data collection with a nominal threshold voltage and the other for efficiency monitoring with a threshold voltage set around the peak of a pulse height distribution (i.e., ~250 mV). The observed efficiency changes over the course of measurements were corrected during data processing.

Oxygen isotopic compositions of small (< 10 μm) grains were analyzed with a primary Cs^+ ion beam of ~30 pA focused to ~2 μm diameter and rastered over 1×1 μm^2 area. Three oxygen isotopes were measured simultaneously: $^{16}O^-$ was measured on a FC and $^{17}O^-$ and $^{18}O^-$ were measured on EMs. Contribution of $^{16}OH^-$ onto $^{17}O^-$ was corrected based on a peak/tail ratio and $^{16}OH^-$ measured during each measurement. The correction was typically less than 0.05‰.

Instrumental fractionation was corrected using terrestrial standards including San Carlos olivine (for melilite and olivine), diopside (for grossmanite, louisfuchsite, and Al,Ti-diopside), Burma spinel (for spinel and hibonite), Miyake-jima anorthite (for plagioclase), and grossular (for grossular). Reported uncertainties reflect the propagation of both the internal analytical precision and the external reproducibility of the standards. Typical uncertainties for $\delta^{18}O$ and $\Delta^{17}O$ were ~0.5 and 0.5‰, and ~1.5 and 2.0‰, for the first and second protocols, respectively. The spots analyzed for oxygen isotopes were verified with secondary and BSE images using the UH JEOL JXA-8500F electron microprobe and/or UH JSM-5900LV SEM after SIMS measurements. Oxygen isotope compositions are reported as $\delta^{17}O$ and $\delta^{18}O$, deviations from Vienna Standard Mean Ocean Water (VSMOW; $^{17}O/^{16}O_{VSMOW} = 0.000380$; $^{18}O/^{16}O_{VSMOW} = 0.002005$; De Laeter et al., 2003) in parts per thousand: $\delta^{17,18}O_{VSMOW} = [(^{17,18}O/_{16}O_{sample})/(^{17,18}O/^{16}O_{VSMOW}) - 1] \times 1000$, and as deviations from the terrestrial fractionation (TF) line, $\Delta^{17}O$.

Aluminum- and magnesium-isotope compositions were measured *in situ* with the UH Cameca ims-1280 SIMS using protocols similar to those in Makide et al. (2009) and Park et al. (2016). Primary $^{16}O^-$ ions were accelerated to −13 keV. Positive secondary ions were accelerated to 10 keV. An energy window of 55 eV was used. Standards used were synthetic

Al-Ti-diopside, synthetic melilite glass, synthetic hibonite, and Burma spinel (NMNH R18112). The standards were analyzed at the beginning and end of each daily run. Minerals with high $^{27}Al/^{24}Mg$ ratios (gehlenitic melilite and hibonite) were analyzed with the $^{16}O^-$ primary beam focused to ~2 μm diameter and a current of ~60–80 pA. Secondary $^{24}Mg^+$, $^{25}Mg^+$, and $^{26}Mg^+$ ions were measured with the monocollection EM in peak jumping mode, and $^{27}Al^+$ ions were measured with a multicollection FC, simultaneously with $^{25}Mg^+$ measurement. Counting times were 4 s for $^{24}Mg^+$ and 10 s for all others; the measurements typically consisted of 120 cycles. Entrance and exit slits were set to obtain the MRP of ~ 3700, sufficient to separate interference ions from Mg-isotope signals. Minerals with low $^{27}Al/^{24}Mg$ ratios (grossmanite and spinel) were analyzed with an $^{16}O^-$ primary beam diameter of ~20 μm and primary current of ~2 nA. Four multicollection FCs were used to detect $^{24}Mg^+$, $^{25}Mg^+$, $^{26}Mg^+$, and $^{27}Al^+$ simultaneously. The MRP was set to ~2400 with exit slits of 500 μm. Although this setting does not allow a complete separation of $^{25}Mg^+$ from $^{24}MgH^+$ interference, the contribution of $^{24}MgH^+$ onto $^{25}Mg^+$ was estimated to be less than 1 ppm. Each analysis consisted of 15 cycles with a counting time of 10 s per cycle.

The measured $^{27}Al^+/^{24}Mg^+$ ratios were corrected using relative sensitivity factors (RSFs) determined from measurements on standards. Mass fractionation was corrected using a standard-sample bracketing to separate instrumental and intrinsic mass fractionation, followed by intrinsic mass fractionation correction using an exponential law with an experimentally determined exponent (Makide et al. 2009; Park et al. 2016). The reported errors (2σ) include both the internal precision of an individual analysis (2SE; two standard error of the mean of measurement cycles) and the external reproducibility for standard measurements (2SD; two standard deviation) during a given analytical session. All isochron slopes and intercepts, and their respective 2σ uncertainties, were determined using IsoPlot and a model-1 fit.

RESULTS

Louisfuchsite occurs with fine-grained rutile and titanite, as irregular grains at 1 to 8 μm in size (Fig. 1), which are the holotype material. It has a light brown colour and is transparent. Its hardness is probably ~5-6, like rhönite. Lustre, streak, tenacity, cleavage, fracture, density, and optical properties could not be determined because of the small grain size. Louisfuchsite is non-cathodoluminescent under the electron beam in an SEM. The calculated density is 3.44 g/cm^3 using the empirical formula. The Gladstone-Dale relationship gives $n = 1.816$.

Louisfuchsite occurs in three regions within the CAI, along with primary spinel, perovskite, grossmanite, plus secondary rutile, titanite, and ilmenite (Fig. 1). Other areas of this CAI, contain spinel, perovskite, grossmanite, Al,Ti-diopside, melilite, hibonite, along with secondary grossular, anorthite, clintonite, wadalite, pentlandite, forsterite, Al-diopside, spinel, and trace of laurite and irarsite. Part of this CAI (~3 mm in size) with a partial Wark-Lovering rim is present in section NWA 4964A. The matrix around the CAI consists mainly of Fe-rich olivine with minor albitic plagioclase, diopside and magnetite.

The empirical formula (based on 20 oxygen atoms *pfu*) of type louisfuchsite is $Ca_{2.00}(Mg_{3.44}Ti^{4+}_{1.49}Fe_{0.36}Ti^{3+}_{0.34}Al_{0.24}V^{3+}_{0.07}Ca_{0.06}Cr_{0.01})_{\sum 6.01}(Al_{3.63}Si_{2.37})_{\sum 6.00}O_{20}$, with Ti^{3+} and Ti^{4+} charge-balanced to achieve ideal stoichiometry. The simplified formula is $Ca_2(Mg,Ti^{4+},Fe,Ti^{3+},Al,V^{3+},Ca)_6(Al,Si)_6O_{20}$. The ideal formula is $Ca_2(Mg_4Ti^{4+}_2)(Al_4Si_2)O_{20}$, which requires Al_2O_3 26.93, MgO 21.29, TiO_2 21.10, SiO_2 15.87, CaO 14.81, total 100.00 wt%. For comparison, the Allende rhönite (louisfuchsite now) in Type A CAIs by Fuchs (1971, 1978) has empirical formulas $Ca_{2.00}(Mg_{2.96}Ti^{4+}_{1.18}Al_{0.74}Ca_{0.43}Ti^{3+}_{0.42}Fe_{0.20}V_{0.07})(Al_{3.58}Si_{2.42})O_{20}$ and $Ca_{2.00}(Mg_{3.29}Ti^{4+}_{1.06}Ti^{3+}_{1.06}Al_{0.42}V_{0.11}Fe_{0.06}Ca_{0.04})(Al_{3.81}Si_{2.19})O_{20}$ (Fuchs 1978), with minor Ti^{3+}, similar to that of type louisfuchsite. Louisfuchsite has Al > Si in the T sites, whereas real rhönite has Al ≤ Si in the T sites.

The EBSD patterns of louisfuchsite can be indexed only by the $P\bar{1}$ aenigmatite structure and give a best fit using the Allende rhönite (louisfuchsite) structure from Bonaccorsi *et al*. (1990) (Fig. 2), with a mean angular deviation of 0.33º to 0.37º; revealing the cell parameters: a = 10.37(1) Å, b = 10.76(1) Å, c = 8.90(1) Å, α = 106.0(1)°, β = 96.0(1)°, γ = 124.7(1)°, V = 741(2) Å^3, and Z = 2. In the crystal chemical formula $Ca_2M_6(Al,Si)_6O_{20}$, the largest cation Ca occupies the M8 and M9 octahedral sites, *M* elements in the M1 to M7 octahedral sites, Al and minor Si in the T1 to T6 tetragonal sites. Among the *M* elements in three cation groups based on the dominant-valency rule, Mg is dominant in louisfuchsite, Al-dominant in addibischoffite, Sc-dominant in warkite, and V-dominant in beckettite (Fig. 3).

The X-ray powder-diffraction data for type louisfuchsite (Table S1, in Å for Cu*K*α1, Bragg-Brentano geometry) are calculated from the cell parameters above, and the atomic coordinates of Bonaccorsi *et al*. (1990) with the empirical formula from this study, using Powder Cell version 2.4.

Oxygen isotopic composition of primary and secondary minerals in the NWA 4964 CTA CAI are listed in Table 2 and plotted in Figures 4a,b. On a three-isotope oxygen diagram, $\delta^{17}O$ *vs.* $\delta^{18}O$, primary grossmanite, hibonite, louisfuchsite, melilite, and spinel plot along a

~slope-1 line. Spinel, hibonite, louisfuchsite, and a grossmanite inclusion in spinel have $\Delta^{17}O$ of ~ –24±2‰ (2SD), whereas coarse grossmanite grains poikilitically enclosing spinel and residual gehlenite enclosing hibonite are similarly ^{16}O-depleted ($\Delta^{17}O$ ~ –6 to –4‰). Secondary grossular, olivine, Al-diopside, and plagioclase plot along mass-dependent fractionation line with $\Delta^{17}O$ of –3.7±1.9‰; $\delta^{18}O$ range from ~ −6 to +4‰.

Aluminum and magnesium isotope data of primary minerals in the NWA 4964 CTA CAI are shown in Table 3. Hibonite, grossmanite, and spinel define an internal Al-Mg isochron with $(^{26}Al/^{27}Al)_0$ of $(5.01\pm0.24)\times10^{-5}$ (Fig. 5). Melilite has high $^{27}Al/^{24}Mg$ ratio (100−700), barely resolvable $^{26}Mg^*$, and does not belong to the isochron.

DISCUSSION

The NWA 4964 CAI #1 is a Compact Type A (CTA) inclusion initially composed of gehlenitic melilite, louisfuchsite, grossmanite, perovskite and Mg-spinel which crystallized from an ^{16}O-rich ($\Delta^{17}O$ ~ –24±2‰) refractory melt with an initial $^{26}Al/^{27}Al$ ratio of $(5.01\pm0.24)\times10^{-5}$ under highly reducing conditions as indicated by high Ti^{3+}/Ti^{4+} ratio in grossmanite (Krot et al. 2023a,b). Subsequently, the CAI experienced an open-system metasomatic alteration by an aqueous fluid with addition of Si, Fe, and Na and local mobilization of Ca, Al, Mg, and Ti, and thermal metamorphism. These processes resulted in nearly complete replacement of melilite by Fe- and Ti-bearing grossular, Fe- and Ti-bearing Al-diopside, clintonite, wadalite, Fe,Mg-spinel, anorthitic plagioclase, and Fe,Mg-olivine. Grossmanite was corroded by Al,Ti-diopside, rutile, and ilmenite. Louisfuchsite and spinel gained some Fe at this stage during fluid-assisted thermal metamorphism. Louisfuchsite and spinel grains enclosed by louisfuchite also exsolved rutile and titanite (Fig. 4c; see also Fig. 2b in Krot et al. 2023a). The residual melilite exsolved a Mg-bearing phase (Fig. 6) that resulted in an increase of Al/Mg ratio and disturbance of its Al-Mg isotope systematics (Fig. 5). Calcium, aluminum, and titanium removed from the CAI were used to form a discontinuous thick layer of secondary Ca±Fe-rich silicates – diopside-hedenbergite solid solution pyroxenes, grossular-almandine solid solution garnets, and minor andradite outside the inclusion (Krot et al. 2023a). Similar metasomatic alteration, but a lesser degree experienced coarse-grained igneous CAIs from the CV>3.6 carbonaceous chondrite Allende (Krot et al. 2021).

Oxygen isotopic compositions of secondary minerals in the coarse-grained igneous CAIs from CK3.7–3.8 chondrites plot along mass-dependent fractionation line with $\Delta^{17}O$ of –3.7±1.9‰ that corresponds to $\Delta^{17}O$ of the CK aqueous fluid (Fig. 4b; Krot et al. 2023b). The

$\Delta^{17}O$ value of the CK aqueous fluid is indistinguishable from that of the Allende aqueous fluid that resulted in metasomatic alteration of its coarse-grained igneous CAIs (Fig. 4d; Krot et al. 2022). In both cases, the metasomatic alteration modified O-isotopic compositions of the same primary minerals in the CTA CAIs – melilite and Ti-rich pyroxenes; hibonite, spinel, louisfuchsite, low-Ti pyroxenes, and Ti-rich pyroxenes enclosed by spinel retained the initial ^{16}O-rich compositions (Figs. 4a, c). The ^{16}O-rich grossmanite is enclosed in spinel with perovskite in one louisfuchsite region (Fig. 7).

IMPLICATIONS

Louisfuchsite is a new member of the rhönite subgroup under the sapphirine supergroup. Louisfuchsite in the NWA 4964 CAI crystallized from an ^{16}O-rich refractory melt with a canonical $^{26}Al/^{27}Al$ of $\sim 5\times10^{-5}$ under reduced solar-like conditions, among the first solid materials to occur in the solar nebula, joining other 50+ refractory minerals identified in carbonaceous chondrites (Rubin and Ma 2021). These refractory minerals mark the very beginning of mineral evolution in the solar system.

ACKNOWLEDGEMENTS

We thank Andrew M. Davis, Robert M. Hazen and Associate Editor Steven B. Simon for their constructive reviews on the manuscript. SEM, EBSD and EPMA were carried out at the Geological and Planetary Science Division Analytical Facility, Caltech, which is supported in part by NSF grants EAR-0318518 and DMR-0080065. This work was also supported the Emerging Worlds NASA grant 80NSSC23K0253 (ANK, PI).

REFERENCES CITED

Armstrong, J.T. (1995) CITZAF: A package of correction programs for the quantitative electron beam X-ray analysis of thick polished materials, thin films, and particles. Microbeam Analysis, 4, 177–200.

Bonaccorsi, E., Merlino, S. and Pasero, M. (1990) Rhönite: structural and microstructural features, crystal chemistry and polysomatic relationships. European Journal of Mineralogy, 2, 203–218.

Clayton, R.N., Onuma, N., Grossman, L. and Mayeda, T.K. (1977) Distribution of the presolar component in Allende and other carbonaceous chondrites. Earth & Planetary Science Letters, 34, 209–224.

De Laeter, J.R., Bohlke, J.K., De Bièvre, P., Hidaka, H., Peiser, H.S., Rosman, K.J.R. and Taylor, P.D.P. (2003) Atomic Weights of the Elements: Review 2000 (IUPAC Technical Report). Pure and Applied Chemistry, 75: 683–800.

Fuchs, L. (1971) Occurrence of wollastonite, rhönite, and andradite in the Allende meteorite. American Mineralogist, 56, 2053–2068.

Fuchs, L. (1978) The mineralogy of a rhönite-bearing calcium aluminum rich inclusion in the Allende meteorite. Meteoritics, 13, 73–88.

Grew, E.S., Halenius, U., Pasero, M. and Barbier J. (2008) Recommended nomenclature for the sapphirine and surinamite groups (sapphirine supargroup). Mineralogical Magazine, 72, 839–876.

Kita, N.T., Hertwig, A.T., Defouilloy, C., Kitajima, K. and Spicuzza, M.J. (2018) Improvements of SIMS Mg isotope analyses for meteoritic and cometary samples using RF Plasma Ion Source. 49th Lunar and Planetary Science Conference, abstract #2441.

Krot, A.N., Petaev, M.I. and Nagashima K. (2021) Infiltration metasomatism of the Allende coarse-grained calcium-aluminum-rich inclusions. *Progress in Earth and Planetary Science*, 8, 61.

Krot, A.N., Nagashima, K., MacPherson, G.J. and Ulyanov, A.A. (2022) On the nature of oxygen-isotope heterogeneity of igneous calcium-aluminum-rich inclusions in CV carbonaceous chondrites. Geochimica et Cosmochimica Acta, 332, 327–354.

Krot, A.N., Dunn, T.L., Petaev, M.I., Ma, C., Nagashima, K. and Zipfel, J. (2023a) Metasomatic alteration of coarse-grained igneous calcium-aluminum-rich inclusions from CK3 carbonaceous chondrites. Meteoritics & Planetary Science, early view. doi.org/10.1111/maps.14080.

Krot, A.N., Nagashima, K., Dunn, T.L., Petaev, M.I. and Ma, C. (2023b) Mineralogy, petrography, oxygen- and aluminum-magnesium isotope systematics of igneous CAIs from CK3 chondrites. 86th Annual Meteoritical Society Meeting, Abstract #6116.

Ma, C. and Krot, A.N. (2014) Louisfuchsite, IMA 2022-024. CNMNC Newsletter 68; Mineralogical Magazine, 86, 856–857.

Ma, C. and Rossman, G.R. (2008) Barioperovskite, $BaTiO_3$, a new mineral from the Benitoite Mine, California. American Mineralogist, 93, 154–157.

Ma, C. and Rossman, G.R. (2009) Tistarite, Ti_2O_3, a new refractory mineral from the Allende meteorite. American Mineralogist, 94, 841–844.

Ma, C., Krot, A.N. and Nagashima, K. (2017) Addibischoffite, $Ca_2Al_6Al_6O_{20}$, a new calcium aluminate mineral from the Acfer 214 CH carbonaceous chondrite: A new refractory phase from the solar nebula. American Mineralogist, 102, 1556–1560.

Ma, C., Krot, A.N., Beckett, J.R., Nagashima, K., Tschauner, O., Rossman, G.R., Simon, S.B. and Bischoff, A. (2020) Warkite, $Ca_2Sc_6Al_6O_{20}$, a new mineral in carbonaceous chondrites and a key-stone phase in ultrarefractory inclusions from the solar nebula. Geochimica et Cosmochimica Acta, 277, 52–86.

Ma, C., Krot, A.N., Paque, J.M., Tschauner, O. and Nagashima, K. (2021) Beckettite, $Ca_2V_6Al_6O_{20}$, a new mineral in a Type A refractory inclusion from Allende and clues to processes in the early solar system. Meteoritics & Planetary Science, 56, 2265–2272.

Makide, K., Nagashima, K., Krot, A.N., Huss, G.R., Hutcheon, I.D. and Bischoff, A. (2009) Oxygen– and magnesium-isotope compositions of calcium–aluminum-rich inclusions from CR2 carbonaceous chondrites. Geochimica et Cosmochimica Acta, 73, 5018−5051.

Nagashima, K., Krot, A.N. and Huss, G.R. (2015) Oxygen-isotope compositions of chondrule silicates and matrix grains in Kakangari K-grouplet chondrite. Geochimica et Cosmochimica Acta, 151, 49–67.

Park, C., Nagashima, K., Krot, A.N., Huss, G.R., Davis, A.M. and Bizzarro, M. (2016) Calcium-aluminum-rich inclusions with fractionation and unidentified nuclear effects (FUN CAIs): II. Heterogeneities of magnesium isotopes and ^{26}Al in the early solar system inferred from in situ high-precision magnesium-isotopic measurements. Geochimica et Cosmochimica Acta, 201, 6–24.

Rubin, A.E. and Ma, C. (2021) Meteorite Mineralogy. Cambridge Planetary Science (26). Cambridge University Press. DOI:10.1017/9781108613767

Simon, S.B., Davis, A.M. and Grossman L. (1999) Origin of compact type A refractory inclusions from CV3 carbonaceous chondrites. Geochimica et Cosmochimica Acta, 63, 1233–1248.

Siron, G., Fukuda, K., Kimura, M., and Kita, N.T. (2021) New constraints from ^{26}Al-^{26}Mg chronology of anorthite bearing chondrules in unequilibrated ordinary chondrites. Geochimica et Cosmochimica Acta, 293, 103–26.

Ushikubo, T., Kimura, M., Kita, N.T. and Valley, J.W. (2012) Primordial oxygen isotope reservoirs of the solar nebula recorded in chondrules in Acfer 094 carbonaceous chondrite. Geochimica et Cosmochimica Acta, 90, 242–264.

323 Table 1. EPMA data (average of 22 analyses) for type louisfuchsite.

324

Constituent	wt%	Range	SD
Al_2O_3	25.48	24.41-26.37	0.43
SiO_2	18.40	18.03-18.70	0.20
MgO	17.92	17.14-18.17	0.25
$^*TiO_2$	15.36	14.84-16.95	0.43
$^*Ti_2O_3$	3.13	3.02-3.45	0.09
CaO	14.92	14.75-15.09	0.09
FeO	3.30	3.07-3.46	0.10
V_2O_3	0.67	0.57-0.76	0.04
Cr_2O_3	0.08	0.01-0.13	0.03
Total	99.26		

325 *Total titanium has been partitioned between Ti^{3+} and Ti^{4+} for charge balance to achieve ideal
326 stoichiometry.
327

328

329 Table 2. Oxygen isotopic compositions of primary and secondary minerals in the NWA 4964
330 (CK3.8) CTA CAI #1.

mineral	spot#	$\delta^{18}O$	2σ	$\delta^{17}O$	2σ	$\Delta^{17}O$	2σ	Suppl. Fig.
primary minerals								
grs	1	-0.5	0.6	-3.2	0.5	-2.9	0.4	SF11
–"–	2	-0.1	0.6	-3.2	0.4	-3.1	0.4	SF11
–"–	3	-0.3	0.6	-3.2	0.4	-3.1	0.4	SF11
–"–	4	-0.5	0.6	-3.3	0.4	-3.1	0.4	SF11
–"–	5	-0.3	0.6	-3.4	0.4	-3.3	0.4	SF11
–"–	6	0.3	0.6	-3.0	0.4	-3.1	0.4	SF11
–"–	7	0.4	0.6	-3.1	0.4	-3.3	0.4	SF11
–"–	14	-0.5	0.6	-3.5	0.4	-3.3	0.4	SF11
–"–	15	0.0	0.6	-3.2	0.4	-3.2	0.4	SF11
–"–	16	0.4	0.6	-3.3	0.4	-3.5	0.4	SF11
–"–	17	0.2	0.6	-3.2	0.4	-3.3	0.4	SF11
–"–	18	0.2	0.6	-3.1	0.4	-3.2	0.4	SF11
grs in sp	1-1	-40.1	1.3	-45.8	2.0	-25.0	1.9	SF7
AlTi-di in pv	1	2.7	1.3	-2.1	2.1	-3.5	2.0	SF8
hib	1	-45.5	1.2	-47.7	2.4	-24.1	2.3	SF9
–"–	2	-46.2	1.2	-48.8	2.6	-24.7	2.5	SF9
–"–	3	-44.3	1.2	-46.4	2.5	-23.3	2.4	SF9
–"–	4	-44.8	1.2	-48.5	2.4	-25.2	2.3	SF3
–"–	5	-45.4	1.3	-48.4	2.1	-24.7	2	SF3
–"–	6	-45.5	1.2	-47.6	2.4	-23.9	2.4	SF3
–"–	7	-45.0	1.3	-46.9	2.4	-23.5	2.4	SF3
–"–	8	-45.9	1.2	-47.2	2.5	-23.3	2.4	SF3
lfh	1-12	-47.4	0.6	-47.7	0.4	-23.1	0.4	SF12
–"–	1-13	-47.1	0.6	-48.1	0.4	-23.6	0.4	SF12
–"–	1-1	-43.8	1.5	-45.0	2.1	-22.2	2.1	SF1
–"–	1-2	-43.3	1.4	-46.3	2.0	-23.8	2.0	SF1
–"–	1-3	-43.2	1.4	-45.9	2.0	-23.4	2.0	SF1
–"–	2-1	-44.3	1.4	-46.2	2.0	-23.1	2.0	SF2
–"–	2-2	-44.4	1.4	-46.1	2.1	-23.0	2.0	SF2
–"–	2-3	-43.5	1.4	-46.0	2.1	-23.4	2.1	SF2
–"–	2-4	-44.3	1.4	-46.3	1.9	-23.2	1.9	SF2
mel	1	-0.8	0.9	-4.4	2.6	-4.0	2.6	SF3
–"–	2	0.4	1.0	-3.3	2.7	-3.5	2.7	SF3
–"–	3	0.5	1.0	-2.7	2.5	-3.0	2.5	SF3
pv	1	-5.1	1.2	-6.1	1.9	-3.5	2.0	SF10
–"–	2	-5.3	1.2	-6.6	2.2	-3.9	2.3	SF10
–"–	3	-5.0	0.9	-7.0	1.9	-4.4	2.0	SF10
–"–	4	-4.5	1.3	-6.2	2.0	-3.8	2.1	SF10

sp	1	-39.1	0.8	-43.6	0.5	-23.3	0.5	SF11
–"–	2	-40.4	0.8	-44.4	0.5	-23.5	0.5	SF11
–"–	3	-39.4	0.7	-43.9	0.5	-23.4	0.4	SF11
–"–	4	-41.2	0.7	-45.0	0.5	-23.6	0.5	SF12
–"–	5	-41.0	0.7	-44.8	0.5	-23.5	0.5	SF12
–"–	6	-40.1	0.8	-44.4	0.4	-23.5	0.4	SF11
–"–	7	-41.5	0.8	-44.9	0.5	-23.3	0.5	SF11
–"–	8	-41.3	0.8	-44.5	0.5	-23.0	0.5	SF11
–"–	9	-40.3	0.8	-44.4	0.4	-23.5	0.4	SF12
Secondary minerals								
Al-di	1-8	-2.4	0.6	-5.7	0.4	-4.4	0.4	SF11
sp+Al-di	1-9	-44.9	0.6	-44.8	0.4	-21.4	0.5	SF11
Al-di	1-10	-1.8	0.6	-5.1	0.4	-4.1	0.4	SF11
–"–	1-11	-2.0	0.6	-5.5	0.4	-4.5	0.4	SF11
–"–	1	1.8	1.3	-3.0	2.0	-3.9	1.9	SF3
–"–	2	3.2	1.4	-2.3	2.0	-4.0	1.9	SF3
–"–	3	2.7	1.5	-1.9	2.0	-3.3	2.0	SF3
–"–	4	2.7	1.4	-2.0	2.2	-3.4	2.2	SF3
–"–	5	2.3	1.3	-1.9	2.1	-3.0	2.1	SF3
–"–	6	1.9	1.4	-2.8	2.1	-3.8	2.0	SF2
–"–	7	1.8	1.4	-2.9	2.0	-3.8	2.0	SF2
–"–	8	1.8	1.5	-2.6	2.4	-3.5	2.4	SF2
–"–	9	2.4	1.4	-2.9	2.3	-4.2	2.3	SF2
–"–	10	2.1	1.4	-2.6	1.9	-3.7	1.8	SF2
–"–	11	2.6	1.4	-2.0	2.2	-3.4	2.1	SF2
–"–	12	2.6	1.4	-1.9	2.3	-3.2	2.3	SF6
–"–	13	3.0	1.4	-3.4	1.9	-5.0	1.9	SF6
–"–	14	3.0	1.4	-1.8	2.1	-3.3	2.1	SF6
–"–	15	1.1	1.3	-1.6	2.1	-2.2	2.1	SF6
–"–	16	1.7	1.4	-1.5	2.1	-2.4	2.0	SF6
–"–	17	1.8	1.5	-1.1	2.5	-2.0	2.5	SF6
–"–	18	1.6	1.4	-2.9	2.2	-3.8	2.2	SF6
–"–	19	12.9	1.4	-3.0	2.0	-9.8	2.0	SF6
–"–	20	1.8	1.4	-1.3	2.1	-2.3	2.1	SF5
–"–	21	1.7	1.4	-3.4	2.1	-4.3	2.0	SF5
–"–	22	2.1	1.5	-2.3	2.4	-3.4	2.4	SF5
–"–	23	3.1	1.3	-3.0	2.0	-4.6	2.0	SF5
–"–	24	2.0	1.5	-1.4	1.9	-2.5	1.9	SF5
–"–	25	2.6	1.4	-1.9	2.0	-3.3	2.0	SF5
–"–	26	3.1	1.3	-1.8	2.2	-3.4	2.1	SF5
–"–	27	2.5	1.3	-1.1	1.9	-2.3	1.8	SF5
–"–	28	2.9	1.5	-0.7	2.0	-2.2	1.9	SF4
–"–	29	3.4	1.4	-2.2	2.1	-3.9	2.1	SF4
–"–	30	2.8	1.5	0.0	2.5	-1.5	2.5	SF4

–"–	31	3.0	1.4	-2.2	2.0	-3.7	2.0	SF4
grl	1	-4.7	1.5	-9.4	4.4	-6.9	4.3	SF4
–"–	2	-4.8	1.4	-7.3	2.5	-4.8	2.5	SF4
–"–	3	-2.0	1.4	-5.5	2.0	-4.5	2.0	SF4
–"–	4	-2.4	1.4	-3.6	2.2	-2.3	2.2	SF4
–"–	5	-2.7	1.5	-4.2	2.1	-2.8	2.1	SF4
–"–	6	-4.9	1.5	-6.8	2.3	-4.2	2.4	SF4
–"–	7	-4.6	1.4	-6.3	2.1	-3.9	2.1	SF5
–"–	8	-3.7	1.3	-5.6	2.3	-3.7	2.3	SF5
–"–	9	-5.1	1.4	-8.1	2.3	-5.5	2.3	SF5
–"–	10	-3.8	1.3	-6.8	2.0	-4.9	2.0	SF4
–"–	11	-5.3	1.3	-6.2	2.3	-3.5	2.3	SF4
–"–	12	-4.5	1.4	-5.0	2.4	-2.7	2.4	SF4
–"–	13	-4.3	1.5	-5.4	2.5	-3.2	2.5	SF4
–"–	14	-4.5	1.4	-5.4	2.6	-3.1	2.6	SF4
–"–	15	-5.3	1.4	-6.2	2.5	-3.5	2.4	SF4
–"–	16	-4.6	1.4	-6.0	2.4	-3.7	2.3	SF4
–"–	17	-4.8	1.5	-6.6	2.2	-4.1	2.2	SF4
–"–	18	-4.7	1.4	-5.2	2.2	-2.7	2.2	SF4
–"–	20	-4.9	1.4	-5.7	2.1	-3.2	2.0	SF2
FeMg-ol	1-1	-0.1	0.8	-3.6	0.4	-3.5	0.5	SF13
–"–	1-2	0.2	0.8	-3.2	0.4	-3.3	0.5	SF13
–"–	1	-0.1	0.8	-3.5	2.5	-3.5	2.6	SF9
–"–	2	-0.7	1.0	-4.2	2.2	-3.9	2.3	SF9
–"–	3	-0.6	0.8	-4.8	2.3	-4.5	2.3	SF2
–"–	4	-0.6	0.9	-5.6	2.3	-5.3	2.4	SF2
An-pl	1	2.0	0.7	-2.9	0.5	-4.0	0.6	SF13

Al-di = Al-diopside; AlTi-di = AlTi-diopside; grl = grossular; grs = grossmanite; hib = hibonite; lfh = louisfuchsite; mel = melilite; ol = olivine; pv = perovskite; sp = spinel.

336 Table 3. Aluminum and magnesium isotope data for the NWA 4964 CTA CAI #1.

mineral	spot	$^{27}Al/^{24}Mg$	2σ	$^{26}Mg/^{24}Mg$	2σ	Suppl. Fig.
grs	1	2.7	0.28	0.139483	0.000080	SF14
-"-	2	2.6	0.27	0.139501	0.000080	SF14
-"-	3	2.7	0.28	0.139450	0.000081	SF14
-"-	4	2.7	0.27	0.139476	0.000079	SF14
-"-	5	2.8	0.28	0.139449	0.000081	SF14
-"-	6	3.0	0.30	0.139479	0.000080	SF14
-"-	7	3.1	0.32	0.139519	0.000082	SF14
hib	1	42.4	1.36	0.141534	0.000217	SF16
-"-	2	28.3	0.90	0.140714	0.000215	SF16
-"-	3	38.3	1.22	0.141352	0.000227	SF16
-"-	4	60.1	2.02	0.142105	0.000260	SF16
-"-	5	25.8	0.82	0.140578	0.000226	SF16
-"-	6	32.5	1.04	0.141041	0.000190	SF16
-"-	7	34.4	1.10	0.141098	0.000199	SF16
mel	1	658.2	25.21	0.141673	0.001305	SF16
-"-	2	122.9	4.13	0.140632	0.000722	SF16
sp	1	2.6	0.26	0.139478	0.000025	SF14
-"-	2	2.6	0.26	0.139467	0.000026	SF14
-"-	3	2.6	0.26	0.139443	0.000022	SF14
-"-	4	2.4	0.24	0.139456	0.000027	SF14
-"-	5	2.4	0.24	0.139446	0.000023	SF15
-"-	6	2.4	0.24	0.139451	0.000024	SF15
-"-	7	2.4	0.24	0.139478	0.000025	SF15

337 grs = grossmanite; hib = hibonite; mel = melilite; sp = spinel.

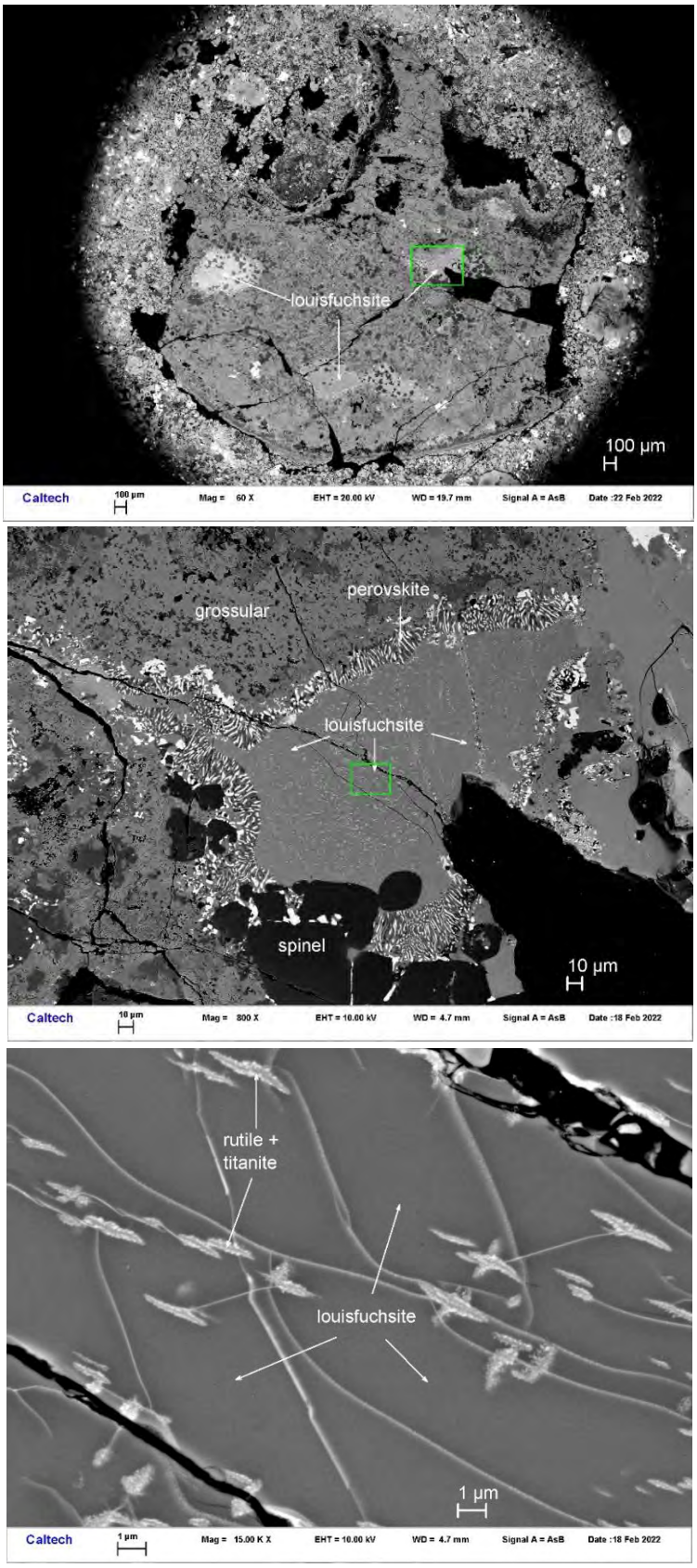

Figure 1. Backscattered electron (BSE) images showing louisfuchsite in a CAI in section NWA 4964A. (a) Overview of the CAI showing three louisfuchsite regions, (b) one louisfuchsite region with a rim of perovskite and spinel, (c) enlarged image showing louisfuchsite with secondary rutile and titanite.

This is the peer-reviewed, final accepted version for American Mineralogist, published by the Mineralogical Society of America.
The published version is subject to change. Cite as Authors (Year) Title. American Mineralogist, in press.
DOI: https://doi.org/10.2138/am-2023-9283. http://www.minsocam.org/

a. b.

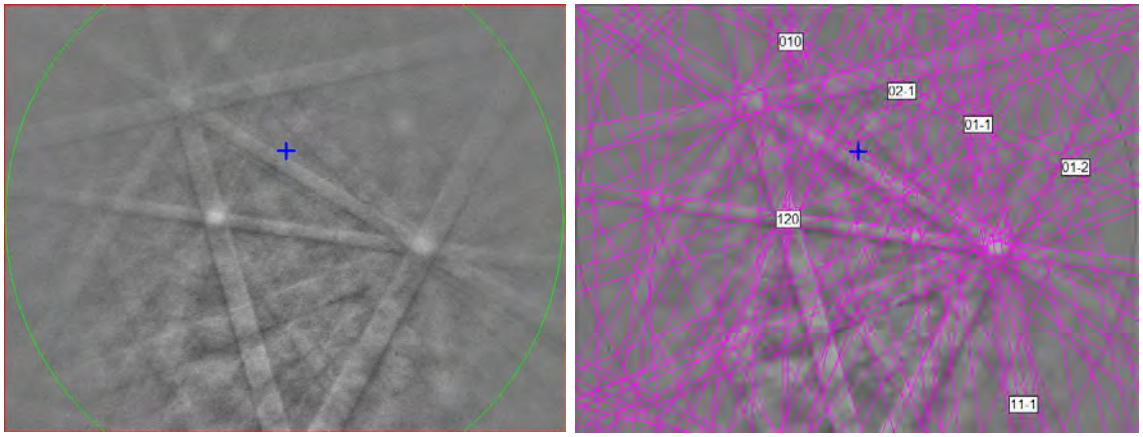

Figure 2. (a) EBSD pattern of one louisfuchsite crystal in Figure 1, and (b) the pattern indexed with the $P\bar{1}$ rhönite structure.

This is the peer-reviewed, final accepted version for American Mineralogist, published by the Mineralogical Society of America.
The published version is subject to change. Cite as Authors (Year) Title. American Mineralogist, in press.
DOI: https://doi.org/10.2138/am-2023-9283. http://www.minsocam.org/

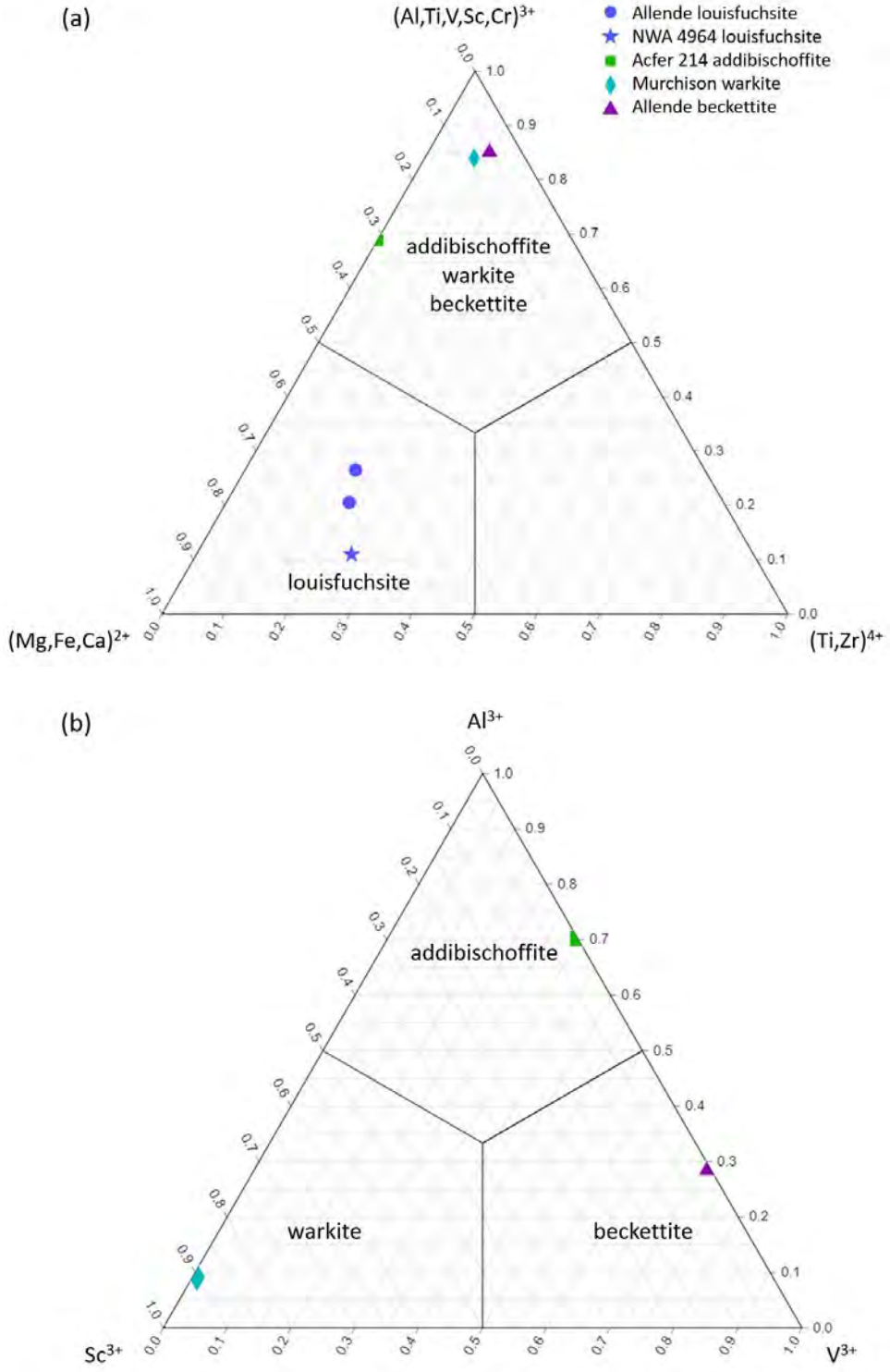

Figure 3. (a) Molar ternary diagram of three cation groups for *M* elements in the crystal chemical formula $Ca_2M_6(Al,Si)_6O_{20}$ from type louisfuchsite in NWA 4964 (this study), the Allende louisfuchsite (Fuchs 1971, 1978), the Acfer 214 addibischoffite (Ma et al. 2017), the Murchison warkite (Ma et al. 2020) and the Allende beckettite (Ma et al. 2021); (b) normalized ternary diagram of Al^{3+}-Sc^{3+}-V^{3+} from addibischoffite, warkite and beckettite where the trivalent cations are dominant.

This is the peer-reviewed, final accepted version for American Mineralogist, published by the Mineralogical Society of America.
The published version is subject to change. Cite as Authors (Year) Title. American Mineralogist, in press.
DOI: https://doi.org/10.2138/am-2023-9283. http://www.minsocam.org/

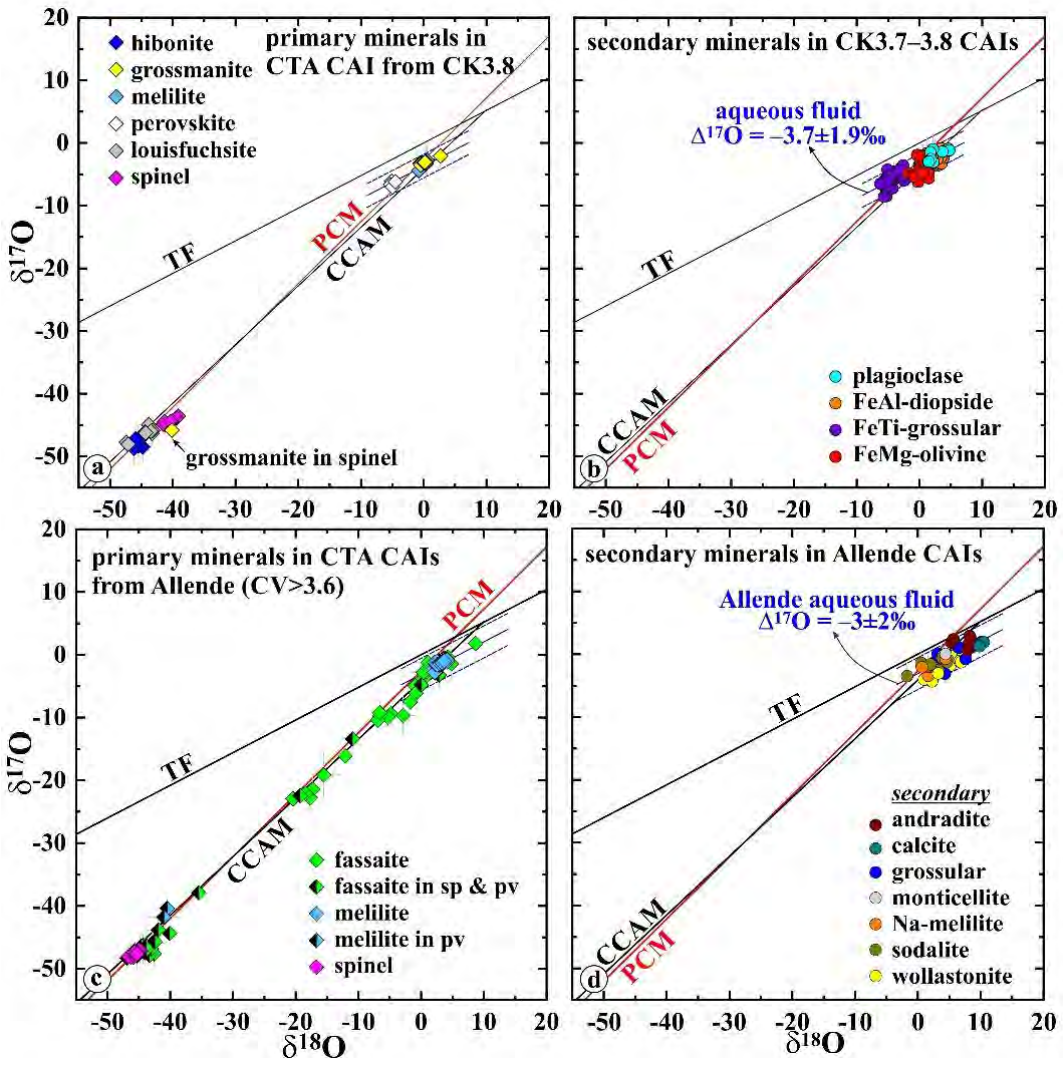

Figure 4. $\delta^{17}O$ *vs.* $\delta^{18}O$ in (a) primary minerals in Compact Type A (CTA) CAI from NWA 4964 (CK3.8), (b) secondary minerals in CTA and Type B CAIs from CK3.7–3.8 chondrites, (c) primary minerals in CTA CAIs from Allende (CV>3.6), and (d) secondary minerals in CTA and Type B CAIs from Allende. Oxygen isotopic compositions of secondary minerals in CK and CV CAIs plot along mass-dependent fractionation lines with $\Delta^{17}O$ (= $\delta^{17}O - 0.52\times\delta^{18}O$) of –3.7±1.9 and –3±2‰, respectively. These $\Delta^{17}O$ values correspond to $\Delta^{17}O$ of aqueous fluids in CK3.7–3.8 and Allende parent bodies. Oxygen isotopic compositions of primary minerals in CK and CV CAIs plot along ~slope-1 line. The NWA 4964 CTA CAI is isotopically heterogeneous: hibonite, spinel, and louisfuchsite have solar-like ^{16}O-rich compositions, whereas melilite and grossmanite (except inclusion in spinel) are ^{16}O-depleted to a level of $\Delta^{17}O$ of the CK aqueous fluid. The Allende CTA CAIs are isotopically heterogeneous: spinel has solar-like ^{16}O-rich composition; whereas melilite and Ti-rich Al,Ti-diopside (fassaite) are ^{16}O-depleted to various degrees. The most ^{16}O-depleted compositions overlap with $\Delta^{17}O$ of the Allende aqueous fluid. CCAM = Carbonaceous Anhydrous Mineral line (Clayton et al., 1977); PCM = Primitive Chondrule Mineral line (Ushikubo et al., 2012); TF = Terrestrial fractionation line. Data for Allende CAIs are from Krot et al. (2022).

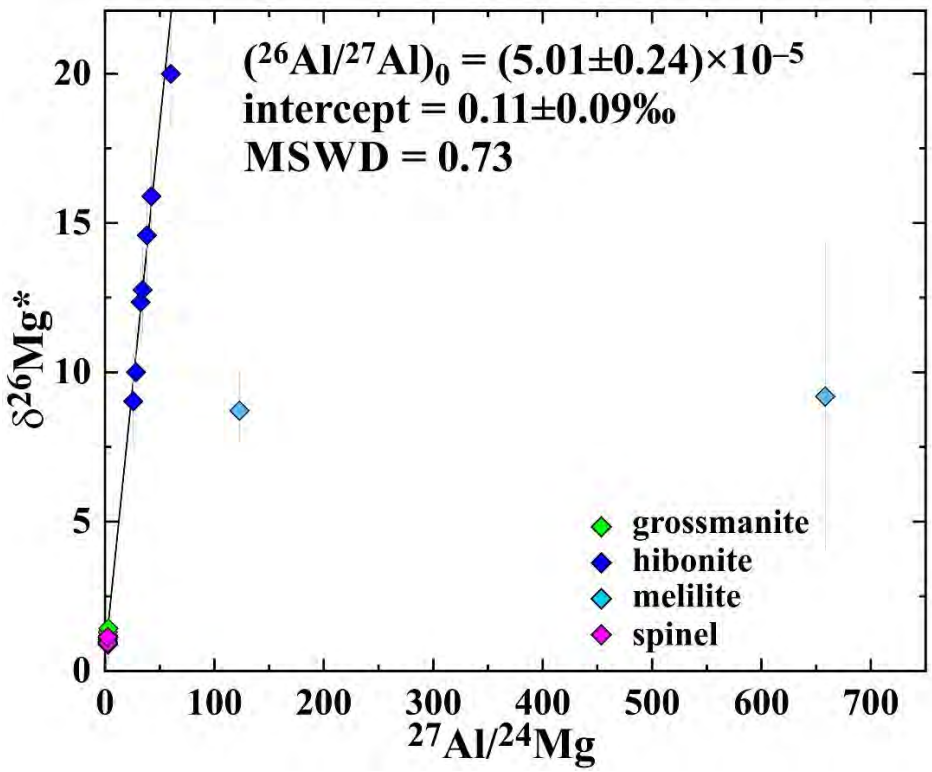

Figure 5. Aluminum-magnesium evolutionary diagram of the CTA CAI from NWA 4964 (CK3.8). Spinel, hibonite, and grossmanite define an internal isochron with $(^{26}Al/^{27}Al)_0 = (5.01\pm0.24)\times10^{-5}$; melilite shows resolvable excess of ^{26}Mg, but has very high $^{27}Al/^{24}Mg$ ratio and does not belong to the isochron. From Krot et al. (2023b).

This is the peer-reviewed, final accepted version for American Mineralogist, published by the Mineralogical Society of America.
The published version is subject to change. Cite as Authors (Year) Title. American Mineralogist, in press.
DOI: https://doi.org/10.2138/am-2023-9283. http://www.minsocam.org/

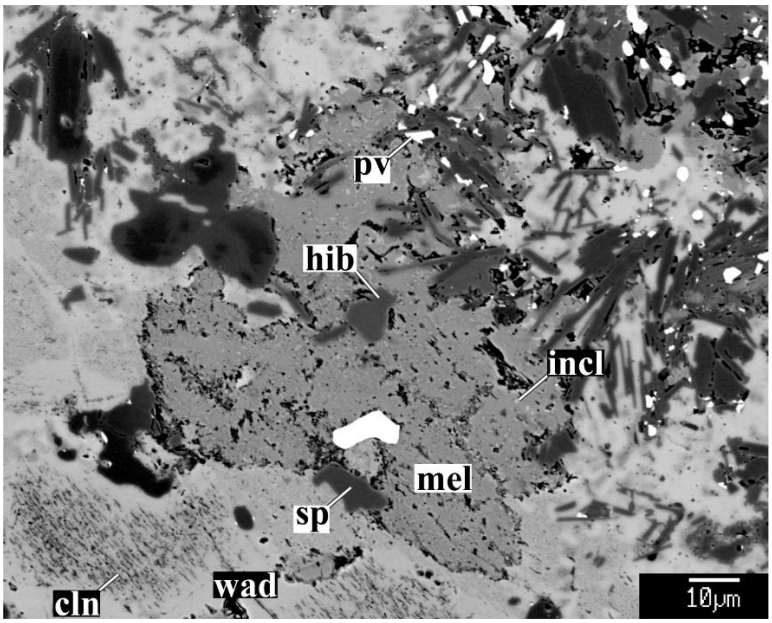

Figure 6. BSE image of residual gehlenitic melilite (mel) poikilitically enclosing hibonite (hib), spinel (sp) and perovskite and containing numerous inclusions (incl) of diopside (?) in the CAI NWA 4964 #1. Melilite is extensively replaced by wadalite (wad) with numerous inclusions of clintonite (cln).

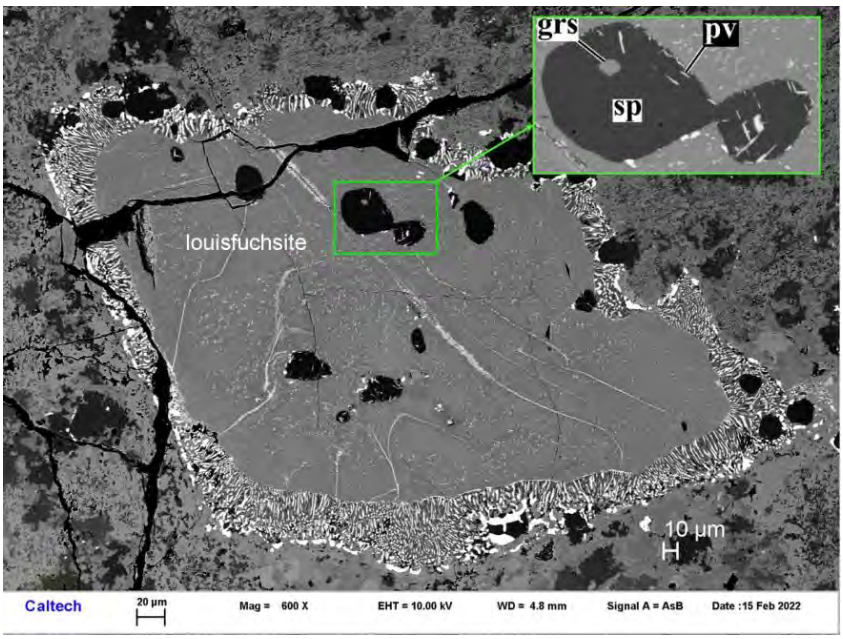

Figure 7. BSE image showing grossmanite (grs) and perovskite (pv) in spinel (sp) in one louisfuchsite region.